Ambient-Pressure XPS Study of a Ni-Fe Electrocatalyst for the Oxygen Evolution Reaction

Harri Ali-Löytty[1,2], Mary W. Louie[3,4,†], Meenesh R. Singh[3,4], Lin Li[1], Hernan G. Sanchez Casalongue[1,‡], Hirohito Ogasawara[5], Ethan J. Crumlin[6], Zhi Liu[6,§], Alexis T. Bell[3,4], Anders Nilsson[1] , and Daniel Friebel[1,]*

[1]SUNCAT Center for Interface Science and Catalysis, SLAC National Accelerator Laboratory, Menlo Park, California 94025, USA

[2]Surface Science Laboratory, Optoelectronics Research Centre, Tampere University of Technology, Tampere 33720, Finland

[3]Department of Chemical and Biomolecular Engineering, University of California, Berkeley, Berkeley, California 94720, USA

[4]Joint Center for Artificial Photosynthesis, Materials Science Division, Lawrence Berkeley National Laboratory, California 94720, USA

[5]Stanford Synchrotron Radiation Light Source (SSRL), SLAC National Accelerator Laboratory, California 94025, USA

[6]Advanced Light Source, Lawrence Berkeley National Laboratory, Berkeley, California 94720, USA

ABSTRACT

Chemical analysis of solid–liquid interfaces under electrochemical conditions has recently become feasible due to the development of new synchrotron radiation techniques. Here we report the use of "tender" X-ray Ambient Pressure X-ray Photoelectron Spectroscopy (APXPS) to characterize a thin film of Ni–Fe oxyhydroxide electrodeposited on Au as the working electrode at different applied potentials in 0.1 M KOH as the electrolyte. Our results show that the as-prepared 7 nm thick Ni–Fe (50% Fe) film contains Fe and Ni in both their metallic as well as oxidized states, and undergoes further oxidation when the sample is subjected to electrochemical oxidation-reduction cycles. Metallic Fe is oxidized to Fe^{3+} and metallic Ni to $Ni^{2+/3+}$.

This work shows that it is possible to monitor the chemical nature of the Ni–Fe catalyst as function of potential when the corresponding current densities are small. This allows for *operando* measurements just above the onset of OER; however, current densities as they are desired in photoelectrochemical devices (~1–10 mA cm^{-2}) could not be achieved in this work, due to ohmic losses in the thin electrolyte film. We use a two-dimensional model to describe- the spatial distribution of the electrochemical potential, current density and pH as a function of the position above the electrolyte meniscus, to provide guidance towards enabling the acquisition of *operando* APXPS at high current density. The shifts in binding energy of water with applied potential predicted by the model is in good agreement with the experimental values.

INTRODUCTION

Solar water splitting is a promising approach to produce hydrogen as a renewable fuel directly from water through a photoelectrochemical reaction on a semiconductor surface.[1] The efficiency of photoelectrochemical devices is largely limited by the slow kinetics of the oxygen evolution reaction (OER), which give rise to substantial overpotentials, defined as the excess potential from the thermodynamic value to run the reaction at a given rate. In response to this challenge, efforts have been undertaken to develop cost-effective electrocatalysts that minimize the required overpotential.[2] The search for superior OER catalysts has been guided by knowledge of structure-performance relationships developed from experimental studies; however, such efforts have lacked direct experimental information on the chemical composition and structure of the solid–liquid interface during the reaction, information that is essential for theoretical modeling of the OER process.[3]

The most promising earth-abundant OER electrocatalysts under alkaline conditions are Ni–Fe oxyhydroxides, which have up to 1000-fold higher OER current densities than pure Fe and Ni oxyhydroxides.[4,5] A recent *operando* X-ray absorption spectroscopy (XAS) and density functional theory investigation of Ni–Fe oxyhydroxides revealed that the active catalyst under OER conditions consists of Fe-doped γ-NiOOH. In this material, Fe occupying Ni sites is highly active, whereas the activity of Ni sites was found to be very low in both pure and Fe-doped γ-NiOOH.[6] Fe sites that share lattice oxide ligands with neighboring Ni sites have near-optimal adsorption energies for the intermediates formed during the OER. To further complement the electronic structure information that was obtained by probing Fe and Ni sites with XAS, we employ here X-ray photoemission spectroscopy (XPS), which can directly probe the chemical state of hydroxide/oxide ligands and species in the electrolytic double layer. The limitation of

XPS to vacuum conditions[7] has been overcome with the recent development of ambient pressure X-ray photoelectron spectroscopy (APXPS) and third generation synchrotron radiation sources that have enabled XPS analysis under electrochemical reaction conditions of solid–gas interfaces in solid-state electrochemical cells,[8,9] at the triple-phase boundary between gas phase, electrolyte and electrocatalyst in proton exchange membrane fuel cells and electrolyzers,[9–11] and at the solid-liquid interface in three-electrode electrochemical cells.[12–14] The latter approach is used here to study a Ni–Fe electrocatalyst for water splitting. Measurements of the binding energy shifts in the O 1s spectrum of H_2O both in the gas and liquid phases were observed as well as shifts in the Ni and Fe core-levels with changes in applied potential. The setup and experimental conditions used for this study enabled observations of changes in the oxidation state of the catalyst and the nature of O-containing species present on the catalyst surface at applied potentials up to and just above the onset of the OER. However, it was not possible to make similar observations under conditions where the OER occurs with a significant current density (> 1 mA/cm^2). A theoretical model of mass transport in the thin electrolyte film was developed to interpret the findings of the present study and as a guide for a further optimized sample cell design that could overcome the limitations of the current setup and operating conditions.

EXPERIMENTAL

Sample preparation

Working electrode substrates were prepared by evaporation of Ti (4 nm) followed by Au (10 nm), using the procedure described by Friebel et al.,[6] onto glass slides that were subsequently cut into 6 x 40 mm^2 strips. Ni–Fe electrocatalysts films were electrodeposited on these conductive substrates from a solution containing 0.01 M nickel sulfate hexahydrate (≥99.99% trace metals

basis, Sigma-Aldrich 467901) and 0.01 M iron sulfate heptahydrate (ACS Reagent ≥99.0%, Sigma-Aldrich 215422) in ultrapure water (18.2 MΩ, EMD Millipore). Ni–Fe films were electrodeposited galvanostatically with a cathodic current density of 50 μA cm^{-2} applied for 113 and 1125 s to obtain 7 and 70 nm thick films, respectively. Electrochemical experiments were conducted in 0.1 M KOH (ACS reagent ≥ 85%, Sigma-Aldrich 221473).

APXPS measurements

APXPS experiments were performed at Beamline 9.3.1 at ALS.[12] The APXPS endstation has a high vacuum analysis chamber equipped with a fast access hatch, an x-y-z sample manipulator, and a differentially pumped high energy electron energy analyzer (VG Scienta R4000 HiPP-2) with a 300 μm diameter entrance nozzle. This system allows XPS measurements to be made under 20 Torr H_2O, the equilibrium vapor pressure of water at room temperature. This vapor pressure of water is needed to minimize the loss of water by evaporation from the thin electrolyte film formed upon withdrawal of the sample from the bulk electrolyte.

The Ni–Fe electrocatalyst sample was attached to the sample manipulator as a working electrode (WE) in a three-electrode configuration shown in Figure 1a with a Pt foil as a counter electrode (CE) and a leak-free Ag/AgCl reference electrode (eDAQ ET072-1) (RE), which were controlled during *operando* XPS measurement with a potentiostat (BioLogic, France). The WE was connected to a common ground with the electron energy analyzer. The WE was positioned approximately 300 μm away from the analyzer entrance nozzle where the XPS count rate was maximized. During electrochemical experiments the electrodes were partly immersed inside a beaker filled with 0.1 M KOH electrolyte solution, and the analysis chamber was backfilled with 18 Torr H_2O using a leak valve.

All spectra were recorded at a photon energy of 4020 eV with an instrumental resolution of 1.1 eV. The inelastic mean free paths (IMFPs, λ) of O 1s photoelectrons with corresponding kinetic energy were 6.0 nm and 9.5 nm in Ni–Fe electrocatalyst (mixed $Ni(OH)_2$ and FeOOH) and liquid H_2O, respectively (Supporting Information). 95% of the XPS signal originates from within 3λ, which is generally referred to as the information depth of XPS. The Au $4f_{7/2}$ peak position was not affected by the applied electrochemical potential and was set to 84.0 eV to calibrate the binding energy scale. The chemical states of elements were determined from XPS spectra by least-squares fitting of Gaussian–Lorentzian lineshapes to the photoelectron peaks after subtracting a Shirley background. The analysis was carried out using CasaXPS software (version 2.3.15).[15]

Operation of the thin film electrochemical cell

Immersion followed by partial retraction of the WE from the electrolyte resulted in the formation of a liquid film on the WE by capillary action. XPS measurements were performed on the WE location where the film was thin enough to enable detection of an XPS signal from the sample, but not too thin for the purpose of preserving the electrical connectivity. This was achieved by adjusting the manipulator height and maintaining the H_2O vapor pressure at ~19 Torr, corresponding to ~100% relative humidity at room temperature.[16]

In order to test whether the XPS-probed region under the thin film electrolyte was under electrochemical potential control, we monitored the change in the local work function, which is equivalent to a change in the electrochemical potential.[17] The work function change can be obtained from the energy shifts of the gas and liquid phase H_2O peak positions in O 1s spectra.[8] These molecules near the surface have core level ionization energies that are constant with respect to the vacuum level but will appear with a peak shift in XPS when the work function is

changed because the XPS binding energy scale is referenced to the Fermi level of the electrode.[18] In addition to the applied external potential, the surface work function is also sensitive to the chemical and structural changes of the surface, which may cause deviation from the 1:1 relation between the applied external potential and the detected binding energy shift of the gas phase molecules. The gas phase peak position is also affected by the electrostatic potential at the site where the ionization takes place, the effect of which was minimized here by grounding the entrance nozzle of the analyzer.[19] The response of the liquid phase peak position to the electrochemical potential will be discussed in detail in the next section. Figure S6 (see Supplementary Information) illustrates the relationship of the various potentials noted above.

Maintaining a stable electrolyte layer was challenging due to the nature of the interaction between the Ni-Fe electrode and the thin electrolyte layer; therefore, special attention was paid to the validation of the XPS data. We collected XPS spectra dynamically by measuring multiple cycles of individual sweeps of O 1s, Ni 2p and Fe 2p regions, to ensure data were collected over a stable thin electrolyte layer. Such "validated" scans were then summed to improve the signal-to-noise ratio. Using this approach, we determined a threshold thickness of approximately 18 nm required to achieve electrochemical potential control of the thin electrolyte film (Supporting Information). For thinner films (< 10 nm), the film became discontinuous to the bulk electrolyte and the potential control was lost; this was accompanied by a strong decrease of the K 2p signal from K^+ ions in the electrolyte, indicating that the electrolyte layer became discontinuous. In contrast, for thicker films (> 30 nm) the substrate signal was lost, which made the quantification of film thickness impossible. The transport of ions within the thin electrolyte layer and the spatial distribution of current density, pH, and potential are discussed in more detail in the next section.

RESULTS AND DISCUSSION

Figure 1a shows a schematic of the thin film electrochemical cell and the sample configuration with respect to the electron energy analyzer at the ALS APXPS beamline 9.3.1. Due to the high kinetic energy (~3–4 keV) and corresponding large information depth (<30 nm) of the photoelectrons, the measured XPS data contain information from four different phases (gas, liquid, Ni–Fe electrocatalyst, Au) and their interfaces. The cyclic voltammogram (CV) of the 7 nm thick Ni–Fe electrocatalyst in 0.1 M KOH electrolyte (Figure 1b)[4,20] shows a reduction peak in the cathodic sweep at 0.35 V vs. Ag/AgCl that originates from reduction of γ-NiOOH to α-Ni(OH)$_2$. The corresponding oxidation wave overlaps with the onset of the oxygen evolution reaction (OER) at potentials greater than 0.47 V vs. Ag/AgCl.[4] The equilibrium potential for OER is 0.26 V vs. Ag/AgCl in 0.1 M KOH. No other characteristic features were detected in the CV. In particular, no redox transition for Au can be detected at ~0.2 V vs. Ag/AgCl indicating that Au does not contribute significantly to the observed electrochemical reactions. This difference to previous studies of similar films deposited atop bulk Au substrates[4] could be attributed to a different surface morphology of the thin Au layer employed here, where a more uniform growth of Ni-Fe catalyst could result in much less electrochemically accessible Au surface area.
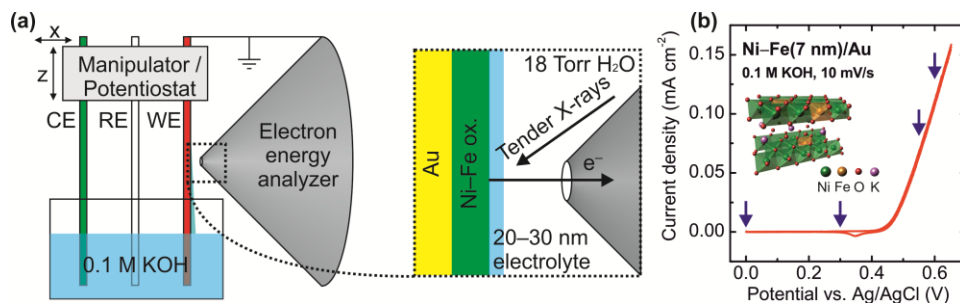

Figure 1. (a) Schematic illustration of the thin film electrochemical cell and the sample configuration. The photoelectrons from the sample penetrate through the liquid electrolyte layer

and surrounding gas phase to the differentially pumped electron energy analyzer. (b) Cyclic voltammogram (CV) of a 7 nm thick electrodeposited Ni–Fe electrocatalyst (50% Fe) layer on an Au substrate. Blue arrows indicate the potentials at which XPS was measured. The inset in (b) shows a structural model for Fe-doped γ-NiOOH.

Figure 2a shows normalized XP spectra of the O 1s region for the Ni–Fe (7 nm) electrocatalyst. The first spectrum was acquired for the as-prepared sample at low humidity (9 Torr). Four different chemical states of oxygen can be clearly distinguished: metal oxides (M–O at 530.1 eV), metal hydroxides (M–OH at 531.6 eV), liquid H_2O (533.0 eV), and gas phase H_2O (536.1 eV).[21,22] Intercalated water within the layered Ni–Fe electrocatalyst is expected to show a peak between those for M–OH and H_2O(l), but this peak could not be distinguished.[23] It is notable that the BE difference between H_2O(l) and H_2O(g) is 3.1 eV on the as-prepared sample at 9 Torr H_2O pressure, and 2.4–2.5 eV on the sample under a ~30 nm liquid electrolyte film; both values are much larger than that observed in XPS measurements of H_2O liquid jets (1.8 eV).[24] Similar deviations can also be seen in other measurements of liquid electrolyte films on conductive surfaces in the same experimental setup.[12] We propose that the electrostatic interaction between the O1s core hole in the liquid electrolyte and its image charge in the metal electrode provides additional screening of the O1s core hole that is not present in liquid jet experiments, resulting in further lowering of the H_2O(l) binding energy.

Subsequently, the sample was fully immersed in 0.1 M KOH, held at 0.65 V vs. Ag/AgCl for 6 min, and then cycled six times between 0 and 0.65 V vs. Ag/AgCl at 10 mV/s. After this treatment, the sample was positioned for XPS (Figure 1a), and spectra were obtained at 0.0 and 0.3 V. Further electrochemical conditioning of the sample was needed before XPS measurements at higher potentials could be made, because it turned out that attempts so far to establish higher

potentials resulted in instabilities of the liquid electrolyte film, which could be noticed by a decrease of the XPS peak intensity from $H_2O(l)$, and loss of local potential control, as determined from the binding energy shifts of electrolyte species and $H_2O(g)$. In order to improve the wetting of the working electrode with electrolyte, the potential cycles were repeated, this time with an increased anodic potential limit, i.e. between 0 and 0.85 V. After this electrochemical conditioning, XPS measurements in the O1s region were repeated at 0.0 V and 0.3 V; O1s, Fe 2p and Ni 2p spectra were obtained at 0.55 V, and additional O1s spectra were also recorded at 0.6 V vs. Ag/AgCl. Under operando conditions, the O 1s signals of the electrocatalyst (M–O and M–OH) were strongly attenuated by the electrolyte film, and the O 1s peak of $H_2O(l)$ dominates the spectra. We note four important observations regarding the peak positions of the $H_2O(g)$ and $H_2O(l)$ components:

(i)   the binding energy difference between $H_2O(g)$ and $H_2O(l)$ decreases from 3.1 eV at 9 Torr to 2.5 eV in the presence of the 0.1 M KOH electrolyte film;

(ii)   upon variation of the potential, both $H_2O(g)$ and $H_2O(l)$ binding energies shift approximately in a linear 1:1 relationship with the applied potential;

(iii)   the history of electrochemical conditioning, i.e., electrochemical potential cycles between 0 and 0.85 V, further affects the $H_2O(g)$/$H_2O(l)$ binding energy difference, which can be seen in Figure 2c to decrease from 2.5 to 2.4 eV;

(iv)   at potentials supporting high current densities above the onset of the OER, $H_2O(g)$ and $H_2O(l)$ binding energy shifts deviate from the 1:1 relationship with applied potential.

The binding energy difference between $H_2O(g)$ and $H_2O(l)$ under electrochemical conditions is reduced compared to the measurement on the humidified sample at 9 Torr, but still larger than

that reported in liquid-jet measurements. We propose that image charges in the metal electrode reduce the binding energy of $H_2O(l)$, and that this effect is stronger in the very thin liquid layer at 9 Torr than in the thick liquid layer, in which the XPS signal originates predominantly from H_2O molecules at a larger distance from the electrode.

The 1:1 relationship of both $H_2O(g)$ and $H_2O(l)$ binding energy shifts with applied potential originates directly from the equivalence of electrochemical potential and work function. The core-level ionization energies of species in the electrolyte and in the gas phase near the electrode surface are referenced to the local vacuum level, whereas the binding energies are measured with respect to the Fermi level. Therefore, electrolyte and gas phase species serve as probes for the local work function.[9,12,14,18]

We propose that small additional changes of the binding energy difference between $H_2O(g)$ and $H_2O(l)$ after potential cycling are induced by changes in the morphology of the Ni-Fe catalyst layer. Potential cycles between 0 and 0.85 V cause redox phase transitions between the Ni(II)/Fe(III) layered double hydroxide structure at low potentials, and Fe(III)/Ni(III)/Ni(IV) oxyhydroxide at high potentials. These repeated phase transitions could cause changes in the size of $(Fe,Ni)O_xH_y$ domains and electrolyte-filled nanopores, and also the local structure of intercalated water and electrolyte ions within such domains. In addition, metallic Fe^0 and Ni^0, which are co-deposited with the hydroxides during sample preparation, undergo irreversible oxidation. These morphological and chemical changes could further reduce the contribution of image charge effects to the screening. At potentials corresponding to OER operating conditions with high current density (> 0.07 mA/cm^2 and 0.1 mA/cm^2 for applied voltages of 0.55 and 0.60 V, respectively), we observe rather significant deviations of both $H_2O(g)$ and $H_2O(l)$ binding energy shifts from the 1:1 relation with applied potential. If we consider, as described above,

species in the liquid electrolyte and in the gas phase as probes of the local work function, these probes can provide a local potential measurement as an ideal reference electrode without any ohmic potential loss, since the resistive path between the probe and the working electrode that can carry electrochemical currents is less than 30 nm long.

Using the same methods as in previous design considerations for photoelectrochemical cells,[25,26] we have developed a two-dimensional model of a dip and pull electrochemical cell (see Supplementary Information, Figure S3), to provide insight into how the current and the transport of species through the meniscus of an electrolyte film of varying thickness can create the observed shift in the binding energy of the O 1s peak for liquid water with applied potential seen in Fig. 2a. The equilibrium shape of meniscus shown in Figure S3b is calculated using a detailed force balance equation (see Supplementary Information). This model is then used to help guide future experiments to reach higher current densities.

Figure S4 shows the variation in the equilibrium potential, kinetic overpotential, and solution losses (sum of ohmic and diffusion losses), as a function of the liquid meniscus height for various applied potentials. Here we see that for large applied potentials (which would support current densities > 0.1 mA/cm^2) the kinetic overpotential decreases to 190 mV at an electrode height of 7 mm, where the solution loss increases to 45 mV and the equilibrium potential increases to 315 mV for an applied potential 0.55 V. The current density decreases to 8 μA cm^{-2} with corresponding decrease of the electrode pH to 12.15, (Figure S5). Figure 2b shows good agreement between experimental and computed values of the shift in binding energy of liquid water.

With this information, we can use the model to propose strategies for minimizing the effects of the ohmic drop in the thin electrolyte layer and enabling APXPS measurements to be made at

current densities of 1-10 mA/cm^2. This could be done by increasing the electrolyte concentration, such as to 1 M KOH, which can increase kinetic overpotential at the XPS position. Another approach would be to use an array of interdigitated microelectrodes with narrow distances between working, counter and reference electrodes, which would lower the solution resistance by several orders of magnitude and therefore enable potential losses due to ohmic resistance to be reduced significantly.
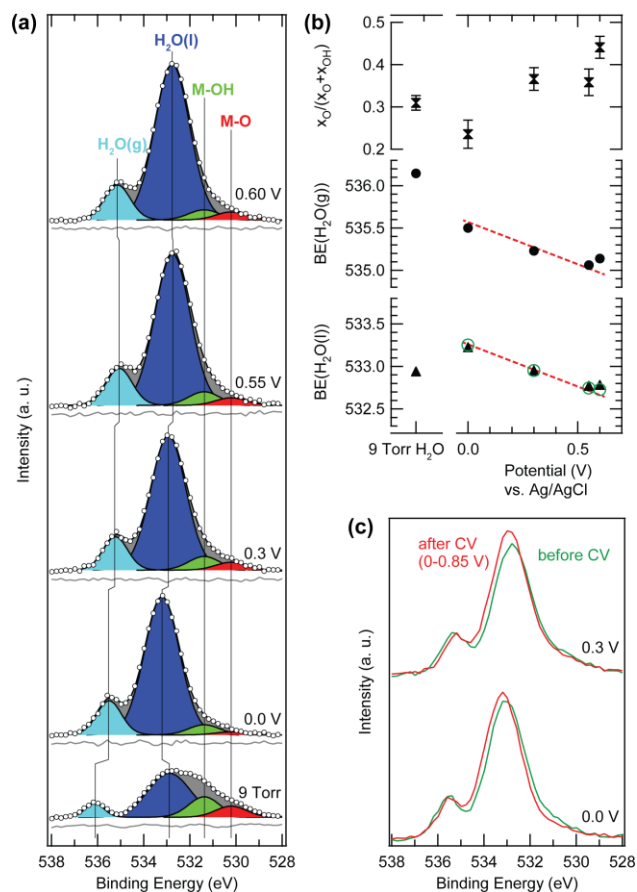

Figure 2. (a) Normalized and background-subtracted O1s XP spectra of Ni–Fe (7 nm) electrocatalyst, excited with 4020 eV X-ray photons. Bottom to top: as-prepared catalyst exposed to 9 Torr H_2O pressure, and operando measurements, taken after extended electrochemical conditioning (6 cycles, 0-0.65 V, and 6 cycles, 0-0.85 V) under a ~30 nm thick 0.1 M KOH liquid film at the indicated applied potentials (vs. Ag/AgCl). The measured spectra (circles) are

fitted with four components (black lines, residuals: gray lines) representing H_2O in the gas and liquid phase, and OH and O in the catalyst. (b) Fit results for spectra in (a): relative intensity of the M–O component in the $MO_x(OH)_y$ catalyst, and measured H_2O peak positions (black symbols) at 9 Torr, and in liquid electrolyte as function of applied potential. The expected 1:1 relationship between peak shift and applied potential is indicated with red dashes, and theoretically modeled peak positions taking into account potential losses in the thin electrolyte layer are shown with green circles. (c) Comparison of XPS measurements taken at identical applied potentials before (green) and after (red) the second electrochemical conditioning (0-0.85 V).

In addition to the energy shifts of H_2O peaks that are induced by the work function change, we observe a significant increase of the relative intensity of the M–O compared to the M–OH peak when the applied potential is increased from 0 to 0.3 V. This could indicate either a transformation of OH to O species in $NiFeO_x(OH)_y$, or the addition of an oxide species due to formation of Au oxide. We note that the observed spectral change is within a potential region where Au electrodes undergo surface oxide formation.[27,28] However, if Au oxidation took place, we would expect the Au 4f spectra to exhibit a new component at ~1 eV higher binding energy; such a spectral change was not detected in our measurements (Figure S7). The additional oxide species appears at a potential at which, according to the cyclic voltammogram, we do not yet expect oxidation of $Ni(OH)_2$ to NiOOH. This is consistent with recent *in situ* Raman measurements within the same potential region, which revealed a spectral signature of NiOOH prior to the oxidation wave in the corresponding voltammogram.[29] Recently, Trześniewski et al. assigned additional weak Raman features at 900–1150 cm^{-1} to "active oxygen" that was proposed to occur as a peroxo species that was anionic, since it was observed only at pH=13 and

14

not in borate buffer at pH=9.2.[30] What is different between the observations here and in ref. 29, and the report by Trześniewski et al. is that the "active oxygen" species was observed along with the oxidation of Ni^{2+} to Ni^{3+}, as indicated by UV-vis and XAS data, whereas the additional oxide species in our study and, likewise, the Raman peak at 560 cm^{-1} in ref. 29, arise before the onset of Ni oxidation. Furthermore, the binding energy at 530.1 eV is too low to account for a peroxo species. Instead, we propose that partial deprotonation of $Ni(OH)_2$ precedes the oxidation of Ni^{2+} to Ni^{3+}, and the resulting negative charge in the $Ni(OH)_{2-x}O_x^{x-}$ layer is stabilized by electrostatic interactions with the electron-depleted Au surface. Due to the poor electron conductivity of $Ni(OH)_2$, it is likely that such an electric double layer at the $Au/Ni(OH)_2$ interface can be formed, in which $Ni(OH)_2$ acts as a solid electrolyte rather than being part of the working electrode.

The relative increase of the M–O intensity after increasing the potential from 0 to 0.3 V was observed both before and after the second electrochemical conditioning of the sample. Besides the 0.1 eV shift of the $H_2O(l)$ peak, we did not find any influence of electrochemical conditioning on the appearance of the M–O and M–OH components (Figure S8).

In Figure 3 we compare the normalized XPS spectra in the Ni and Fe 2p regions for the Ni–Fe film after electrodeposition (bottom spectrum) to those collected after electrochemical conditioning and under electrochemical potential control at 0.3 and 0.55 V vs. Ag/AgCl. The Ni $2p_{3/2}$ spectrum obtained after electrodeposition was fitted using three components: a narrow peak at 852.56 eV corresponding to metallic Ni and two broader peaks at 855.73 and 861.28 eV corresponding to the main and satellite peaks of oxidized $Ni^{2+/3+}$, respectively.[22] The Fe $2p_{3/2}$ spectrum was fitted using four components at 706.64 eV (Fe^0), 709.54 eV (Fe^{2+}), 711.64 eV (Fe^{3+}), and 715.66 eV (satellite of Fe^{2+}).[22] After electrochemical conditioning and under electrochemical potential control at 0.3 V vs. Ag/AgCl, the peaks for Fe^0, Fe^{2+}, and most of the

intensity from metallic Ni^0 disappears, indicating oxidation of the Ni–Fe electrocatalyst throughout its 7 nm thickness. In the case of Fe, the oxidation of Fe species to Fe^{3+} was complete. An increase in potential to 0.55 V (i.e., ~0.45 V at the XPS measurement position), did not result in any notable changes in the Ni and Fe $2p_{3/2}$ spectra.

The binding energies for Ni $2p_{3/2}$ in different Ni oxides and hydroxides taken from the literature are as follows: 852.54 eV (Ni^0), 853.78 eV (NiO), 855.80 eV ($Ni(OH)_2$), and 855.75 eV (γ-NiOOH).[31] Oxide compounds with Ni^{4+} are rare but, for example, a binding energy of 855.1 eV for Ni^{4+} in $Li_{0.10}NiO_2$ has been reported.[32] The observed binding energies for Ni $2p_{3/2}$ at 0.3 and 0.55 V correspond to either $Ni(OH)_2$ or γ-NiOOH where Ni has average oxidation state of 2+ and 3.65+, respectively. The Ni $2p_{3/2}$ peak position is not sensitive enough to differentiate these two compounds from each other, and therefore assignment of Ni oxidation states between 2+ and 4+ is unreliable. Furthermore, due to the multiplet splitting of Ni $2p_{3/2}$, the assignment of a single binding energy value for a chemical compound can be misleading, and in particular, γ-NiOOH has been reported to have a predominance of intensity at higher binding energy in the main line.[33] Therefore, the XPS data of Ni 2p alone cannot rule out the possibility that a fraction of $Ni(OH)_2$ could have been oxidized to γ-NiOOH at the onset of OER. NiOOH formation is further supported by the observed increase of the M–O component in Figure 2.
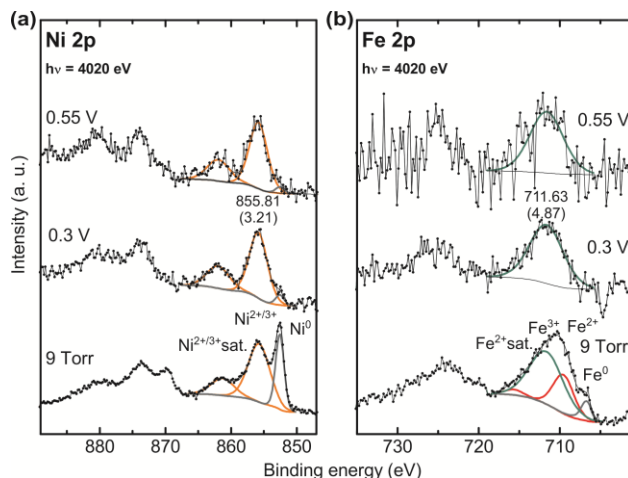
Figure 3. Normalized XP spectra of (a) Ni 2p and (b) Fe 2p transitions for a Ni–Fe (7 nm) electrocatalyst, recorded with 4020 eV excitation energy. Bottom to top in (a) and (b): as-prepared catalyst at 9 Torr H_2O pressure, measurement in 0.1 M KOH at 0.3 V after electrochemical conditioning (6 potential cycles from 0 to 0.65 V), measurement at 0.55 V after additional electrochemical conditioning (6 potential cycles from 0 to 0.85 V).

CONCLUSIONS

We have used *operando* characterization of the surface of a working Ni–Fe electrocatalyst for the OER using "tender" Ambient Pressure X-ray Photoelectron Spectroscopy (APXPS). The catalyst was first immersed in a 0.1 M KOH solution and then partially withdrawn from the electrolyte leaving a meniscus and the catalyst covered with a ~ 30 nm of electrolyte in the XPS probing region. The binding energy shift of species in the electrolyte ($H_2O(l)$ and, not shown here, K^+) and in the gas phase ($H_2O(g)$) can be used to probe the work function change in the XPS probing region; this is a local probe of the electrochemical potential that intrinsically corrects for resistive losses in the thin liquid film. We observe an increase of the O/OH ratio upon potential increase from 0 to 0.3 V, which could be due to initial stages of the oxidation of $Ni(OH)_2$ to NiOOH. Unfortunately, measurements in the Ni 2p region remain somewhat

inconclusive due to the very similar binding energies of Ni^{2+} and Ni^{3+} cations. The use of a planar electrode allowed *operando* XPS measurements just above the equilibrium potential of the OER, with an estimated OER current density within the XPS measurement region of 8 μA/cm^2. Currently, this poses a limitation to the application of APXPS as an operando probe of OER catalysts at current densities where a significant rate of O_2 production can take place. Results from our recent XAS study, in which (Ni,Fe)OOH catalysts were characterized during OER operating conditions at 10 mA/cm^2 and beyond, show that the catalyst is fully oxidized to Fe-doped γ-NiOOH at high OER currents, whereas Ni oxidation is incomplete near the OER onset potential.[6] Alternative approaches are proposed to help facilitate collecting APXPS at high current densities (> 0.1 mA/cm^2), and thereby avoid the limitations caused by the large ohmic loss occurring within the 18–30 nm thick electrolyte film when the XPS measurement position is located more than 0.5 cm above the point of contact of the film with the bulk electrolyte. Strategies to support high current density measurements include raising the electrolyte concentration to 1.0 M and using interdigitated electrode arrays to minimize the distance that electrochemical currents need to pass through the thin electrolyte film.

ASSOCIATED CONTENT

Supporting Information. Additional XPS measurements used to determine if electrochemical potential control was maintained or lost, method for determination of electrolyte thickness, alternative model using electrolyte depletion to account for the XPS O 1s peak position, and video taken inside the APXPS chamber during the OER. This material is available free of charge via the Internet at http://pubs.acs.org.

AUTHOR INFORMATION

Corresponding Author

*Mailing address: SUNCAT Center for Interface Science and Catalysis, SLAC National Accelerator Laboratory, 2575 Sand Hill Road, MS31, Menlo Park, CA 94025, USA. dfriebel@slac.stanford.edu.

Author contributions

H. A.-L. and M. W. L. equally contributed to this work.

Present Addresses

[†] Present address: Exponent, Materials and Corrosion Engineering, 149 Commonwealth Drive, Menlo Park, California 94025, mlouie@exponent.com

[‡] Present address: Exponent, Polymer Science and Materials Chemistry, 149 Commonwealth Drive, Menlo Park, California 94025, hsanchez@exponent.com

Author Contributions

The manuscript was written with contributions from all authors. All authors have given approval to the final version of the manuscript.

REFERENCES

(1) McKone, J. R.; Lewis, N. S.; Gray, H. B. Will Solar-Driven Water-Splitting Devices See the Light of Day? *Chem. Mater.* **2014**, *26* (1), 407–414.

(2) Walter, M. G.; Warren, E. L.; McKone, J. R.; Boettcher, S. W.; Mi, Q.; Santori, E. A.; Lewis, N. S. Solar Water Splitting Cells. *Chem. Rev.* **2010**, *110* (11), 6446–6473.

(3) Man, I. C.; Su, H.-Y.; Calle-Vallejo, F.; Hansen, H. A.; Martínez, J. I.; Inoglu, N. G.; Kitchin, J.; Jaramillo, T. F.; Nørskov, J. K.; Rossmeisl, J. Universality in Oxygen Evolution Electrocatalysis on Oxide Surfaces. *ChemCatChem* **2011**, *3* (7), 1159–1165.

(4) Louie, M. W.; Bell, A. T. An Investigation of Thin-Film Ni–Fe Oxide Catalysts for the Electrochemical Evolution of Oxygen. *J. Am. Chem. Soc.* **2013**, *135* (33), 12329–12337.

(5) Trotochaud, L.; Young, S. L.; Ranney, J. K.; Boettcher, S. W. Nickel–Iron Oxyhydroxide Oxygen-Evolution Electrocatalysts: The Role of Intentional and Incidental Iron Incorporation. *J. Am. Chem. Soc.* **2014**, *136* (18), 6744–6753.

(6) Friebel, D.; Louie, M. W.; Bajdich, M.; Sanwald, K. E.; Cai, Y.; Wise, A. M.; Cheng, M.-J.; Sokaras, D.; Weng, T.-C.; Alonso-Mori, R.; et al. Identification of Highly Active Fe Sites in (Ni,Fe)OOH for Electrocatalytic Water Splitting. *J. Am. Chem. Soc.* **2015**, *137* (3), 1305–1313.

(7) Salmeron, M.; Schlögl, R. Ambient Pressure Photoelectron Spectroscopy: A New Tool for Surface Science and Nanotechnology. *Surf. Sci. Rep.* **2008**, *63* (4), 169–199.

(8) Crumlin, E. J.; Bluhm, H.; Liu, Z. In Situ Investigation of Electrochemical Devices Using Ambient Pressure Photoelectron Spectroscopy. *J. Electron Spectrosc. Relat. Phenom.* **2013**, *190, Part A*, 84–92.

(9) Casalongue, H. S.; Kaya, S.; Viswanathan, V.; Miller, D. J.; Friebel, D.; Hansen, H. A.; Nørskov, J. K.; Nilsson, A.; Ogasawara, H. Direct Observation of the Oxygenated Species during Oxygen Reduction on a Platinum Fuel Cell Cathode. *Nat. Commun.* **2013**, *4*.

(10) Sanchez Casalongue, H. G.; Ng, M. L.; Kaya, S.; Friebel, D.; Ogasawara, H.; Nilsson, A. In Situ Observation of Surface Species on Iridium Oxide Nanoparticles during the Oxygen Evolution Reaction. *Angew. Chem. Int. Ed.* **2014**, *53* (28), 7169–7172.

(11) Casalongue, H. G. S.; Benck, J. D.; Tsai, C.; Karlsson, R. K. B.; Kaya, S.; Ng, M. L.; Pettersson, L. G. M.; Abild-Pedersen, F.; Nørskov, J. K.; Ogasawara, H.; et al. Operando Characterization of an Amorphous Molybdenum Sulfide Nanoparticle Catalyst during the Hydrogen Evolution Reaction. *J. Phys. Chem. C* **2014**, *118* (50), 29252–29259.

(12) Axnanda, S.; Crumlin, E. J.; Mao, B.; Rani, S.; Chang, R.; Karlsson, P. G.; Edwards, M. O. M.; Lundqvist, M.; Moberg, R.; Ross, P.; et al. Using "Tender" X-Ray Ambient Pressure X-Ray Photoelectron Spectroscopy as A Direct Probe of Solid-Liquid Interface. *Sci. Rep.* **2015**, *5*.

(13) Karslioglu, O.; Nemsak, S.; Zegkinoglou, I.; Shavorskiy, A.; Hartl, M.; Salmassi, F.; Gullikson, E.; Ng, M.-L.; Rameshan, C.; Rude, B.; et al. Aqueous Solution/Metal Interfaces Investigated in Operando by Photoelectron Spectroscopy. *Faraday Discuss.* **2015**.

(14) Lichterman, M. F.; Hu, S.; Richter, M. H.; Crumlin, E. J.; Axnanda, S.; Favaro, M.; Drisdell, W.; Hussain, Z.; Mayer, T.; Brunschwig, B. S.; et al. Direct Observation of the Energetics at a Semiconductor/liquid Junction by Operando X-Ray Photoelectron Spectroscopy. *Energy Environ. Sci.* **2015**, *8* (8), 2409–2416.

(15) Fairley, N. *CasaXPS: Spectrum Processing Software for XPS, AES and SIMS*; 2009; Vol. Version 2.3.15.

(16) Frank Ogletree, D.; Bluhm, H.; Hebenstreit, E. D.; Salmeron, M. Photoelectron Spectroscopy under Ambient Pressure and Temperature Conditions. *Nucl. Instrum. Methods Phys. Res. Sect. Accel. Spectrometers Detect. Assoc. Equip.* **2009**, *601* (1–2), 151–160.

(17) Kolb, D. M. Electrochemical Surface Science: Past, Present and Future. *J. Solid State Electrochem.* **2011**, *15* (7-8), 1391–1399.

(18) Axnanda, S.; Scheele, M.; Crumlin, E.; Mao, B.; Chang, R.; Rani, S.; Faiz, M.; Wang, S.; Alivisatos, A. P.; Liu, Z. Direct Work Function Measurement by Gas Phase Photoelectron Spectroscopy and Its Application on PbS Nanoparticles. *Nano Lett.* **2013**, *13* (12), 6176–6182.

(19) Siegbahn, H. Electron Spectroscopy for Chemical Analysis of Liquids and Solutions. *J. Phys. Chem.* **1985**, *89* (6), 897–909.

(20) Morishita, M.; Ochiai, S.; Kakeya, T.; Ozaki, T.; Kawabe, Y.; Watada, M.; Tanase, S.; Sakai, T. Structural Analysis by Synchrotron XRD and XAFS for Manganese-Substituted α - and β -Type Nickel Hydroxide Electrode. *J. Electrochem. Soc.* **2008**, *155* (12), A936–A944.

(21) Yamamoto, S.; Kendelewicz, T.; Newberg, J. T.; Ketteler, G.; Starr, D. E.; Mysak, E. R.; Andersson, K. J.; Ogasawara, H.; Bluhm, H.; Salmeron, M.; et al. Water Adsorption on α-Fe$_2$O$_3$ (0001) at near Ambient Conditions. *J. Phys. Chem. C* **2010**, *114* (5), 2256–2266.

(22) Biesinger, M. C.; Payne, B. P.; Grosvenor, A. P.; Lau, L. W. M.; Gerson, A. R.; Smart, R. S. C. Resolving Surface Chemical States in XPS Analysis of First Row Transition Metals, Oxides and Hydroxides: Cr, Mn, Fe, Co and Ni. *Appl. Surf. Sci.* **2011**, *257* (7), 2717–2730.

(23) Payne, B. P.; Biesinger, M. C.; McIntyre, N. S. Use of Oxygen/nickel Ratios in the XPS Characterisation of Oxide Phases on Nickel Metal and Nickel Alloy Surfaces. *J. Electron Spectrosc. Relat. Phenom.* **2012**, *185* (5–7), 159–166.

(24) Winter, B.; Aziz, E. F.; Hergenhahn, U.; Faubel, M.; Hertel, I. V. Hydrogen Bonds in Liquid Water Studied by Photoelectron Spectroscopy. *J. Chem. Phys.* **2007**, *126* (12), 124504.

(25) Singh, M. R.; Stevens, J. C.; Weber, A. Z. Design of Membrane-Encapsulated Wireless Photoelectrochemical Cells for Hydrogen Production. *J. Electrochem. Soc.* **2014**, *161* (8), E3283–E3296.

(26) Jin, J.; Walczak, K.; Singh, M. R.; Karp, C.; Lewis, N. S.; Xiang, C. An Experimental and Modeling/simulation-Based Evaluation of the Efficiency and Operational Performance Characteristics of an Integrated, Membrane-Free, Neutral pH Solar-Driven Water-Splitting System. *Energy Environ. Sci.* **2014**, *7* (10), 3371–3380.

(27) Cherevko, S.; Zeradjanin, A. R.; Keeley, G. P.; Mayrhofer, K. J. J. A Comparative Study on Gold and Platinum Dissolution in Acidic and Alkaline Media. *J. Electrochem. Soc.* **2014**, *161* (12), H822–H830.

(28) Klaus, S.; Trotochaud, L.; Cheng, M.-J.; Head-Gordon, M.; Bell, A. T. Experimental and Computational Evidence of Highly Active Fe Impurity Sites on the Surface of Oxidized Au for the Electrocatalytic Oxidation of Water in Basic Media. *ChemElectroChem* **2015**, n/a – n/a.

(29) Klaus, S.; Cai, Y.; Louie, M. W.; Trotochaud, L.; Bell, A. T. Effects of Fe Electrolyte Impurities on Ni(OH)2/NiOOH Structure and Oxygen Evolution Activity. *J. Phys. Chem. C* **2015**, *119* (13), 7243–7254.

(30) Trześniewski, B. J.; Diaz-Morales, O.; Vermaas, D. A.; Longo, A.; Bras, W.; Koper, M. T. M.; Smith, W. A. In Situ Observation of Active Oxygen Species in Fe-Containing Ni-Based Oxygen Evolution Catalysts: The Effect of pH on Electrochemical Activity. *J. Am. Chem. Soc.* **2015**, *137* (48), 15112–15121.

(31) Biesinger, M. C.; Lau, L. W. M.; Gerson, A. R.; Smart, R. S. C. The Role of the Auger Parameter in XPS Studies of Nickel Metal, Halides and Oxides. *Phys. Chem. Chem. Phys.* **2012**, *14* (7), 2434–2442.

(32) Arai, H.; Tsuda, M.; Saito, K.; Hayashi, M.; Takei, K.; Sakurai, Y. Structural and Thermal Characteristics of Nickel Dioxide Derived from LiNiO2. *J. Solid State Chem.* **2002**, *163* (1), 340–349.

(33) Grosvenor, A. P.; Biesinger, M. C.; Smart, R. S. C.; McIntyre, N. S. New Interpretations of XPS Spectra of Nickel Metal and Oxides. *Surf. Sci.* **2006**, *600* (9), 1771–1779.

TABLE OF CONTENTS GRAPHIC
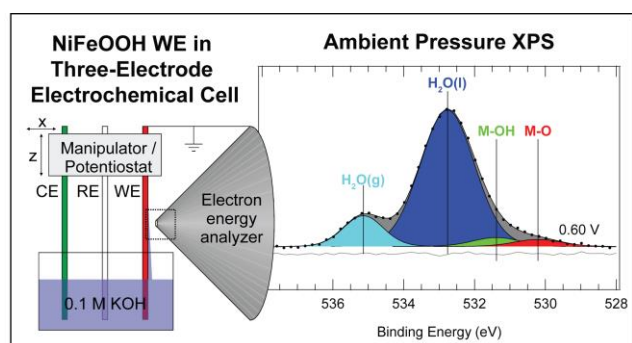
Supporting Information:

Ambient-Pressure XPS Study of a Ni-Fe Electrocatalyst for the Oxygen Evolution Reaction

Harri Ali-Löytty[1,2], Mary W. Louie[3,4,†], Meenesh R. Singh[3,4], Lin Li[1], Hernan G. Sanchez

Casalongue[1,‡], Hirohito Ogasawara[5], Ethan J. Crumlin[6], Zhi Liu[6,§], Alexis T. Bell[3,4], Anders

Nilsson[1], and Daniel Friebel[1]*

[1]SUNCAT Center for Interface Science and Catalysis, SLAC National Accelerator Laboratory, Menlo Park, California 94025, USA

[2]Surface Science Laboratory, Optoelectronics Research Centre, Tampere University of Technology, Tampere 33720, Finland

[3]Department of Chemical and Biomolecular Engineering, University of California, Berkeley, Berkeley, California 94720, USA

[4]Joint Center for Artificial Photosynthesis, Materials Science Division, Lawrence Berkeley National Laboratory, California 94720, USA

[5]Stanford Synchrotron Radiation Light Source (SSRL), SLAC National Accelerator Laboratory, California 94025, USA

[6]Advanced Light Source, Lawrence Berkeley National Laboratory, Berkeley, California 94720, USA

Validation of XPS data under electrochemical potential control

Electrochemical (EC) potential control of the thin film electrolyte was confirmed by monitoring the H_2O gas phase peak shift, i.e. sample work function change, in O 1s spectra, shown in Figure S1(a), with respect to applied potential. For too thin electrolyte layer the potential control was lost, which was accompanied by the strong attenuation of K 2p signal of K+ ions (Figure S1(b)).
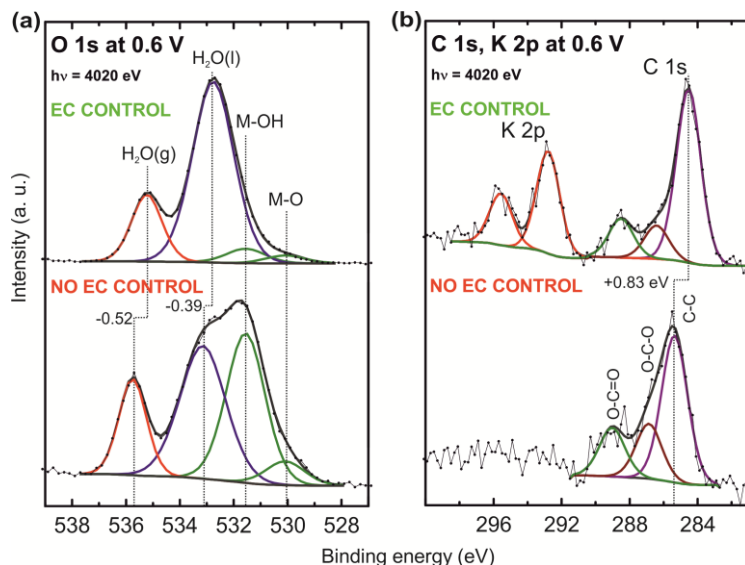

Figure S1. Normalized XPS spectra of (a) O 1s, (b) C 1s and K 2p transitions of Ni–Fe(70 nm) electrocatalyst excited using 4020 eV hard X-ray photons. All the spectra were recorder at 0.60 V (vs. Ag/AgCl) in 0.1 M KOH electrolyte solution. For too thin $H_2O(l)$ layers the electrochemical potential control was lost (NO EC CONTROL), which was accompanied by the attenuation of K 2p signal of K+ ions (b).

The thickness of liquid water layer on electrode based on XPS peak areas can be derived from Beer-Lambert attenuation law, see e.g. ref. [1]:

$$t_{H2O} = \lambda_{H2O} \ln\left(1 + \frac{I_{H2O}}{I_{OX+OH}} \frac{N_{OX+OH}\lambda_{OX+OH}}{N_{H2O}\lambda_{H2O}}\right), \tag{S1}$$

where λ_x is IMFP, I_x is O 1s XPS peak area of component x, N_x number of atoms per unit volume for component x. IMFP values were calculated using TPP2M equation, where 6.9 eV was used as the bandgap for H_2O [2]. For N_{OX+OH} and λ_{OX+OH} we used 55.5 nm^{-3} and 6.0 nm that are average values of $Ni(OH)_2$ and FeOOH, respectively. For N_{H2O} and λ_{H2O} we used 33.4 nm^{-3} and 9.46 nm, respectively. Note that the gas phase H_2O attenuates substrate and liquid phase XPS signals equally, and therefore, liquid water layer thickness can be calculated based on liquid H_2O and substrate signal only.

Fig. S2 shows H_2O layer thickness vs. $H_2O(g)$ XPS peak position in series of O 1s spectra for Ni–Fe(70 nm) electrocatalyst. Threshold thickness for the thin electrolyte layer to maintain mass transfer under applied potential conditions was approximated to be 18 nm. Below this threshold

thickness the electrolyte film was found to be too thin or electrically disconnected to maintain mass transfer required for the electrochemical potential control.
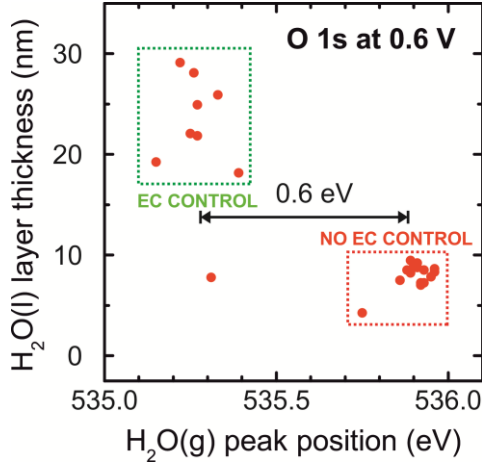

Figure S2. Electrochemical potential control of thin aqueous electrolyte films - H_2O layer thickness vs. $H_2O(g)$ XPS peak position in series of O 1s spectra for Ni–Fe(70 nm) electrocatalyst. All spectra were recorded at 0.60 V (vs. Ag/AgCl) in 0.1 M KOH electrolyte solution.

Theoretical Modeling of "Dipstick" Electrochemical Cell

A two-dimensional model of a "dipstick" electrochemical cell is developed here to explain the observed shift in the binding energy of O 1s peak of liquid water with increase in the applied potential. Figure S3a shows the cross-section of the thin-film of 0.1 M KOH (pH 13) electrolyte attached to the Ni-Fe (50% Fe) anode. The equilibrium shape of the liquid meniscus, which is shown in Figure S3b, is obtained by solving the force balance equation

$$\gamma \frac{d^2h}{dx^2} = \rho \, g \, h \left[1 + \left(\frac{dh}{dx} \right)^2 \right]^{3/2} \tag{S2}$$

where h is the height of the liquid at a distance x from the electrode, γ is the surface tension of gas-liquid interface, ρ is the density of liquid, and g is the acceleration due to gravity. The solution of the equation S2 can be written as

$$\frac{x}{a} = 2 \left[\sqrt{\frac{1-\sin\theta}{2}} - \sqrt{1 - \frac{h^2}{4a^2}} \right] + \ln \left[\frac{a\sqrt{2(1-\sin\theta)} \left(1 + \sqrt{1 - \frac{h^2}{4a^2}} \right)}{h \left(1 + \sqrt{\frac{1-\sin\theta}{2}} \right)} \right] \tag{S3}$$

where θ is the contact angle of liquid with electrode, and $a = \sqrt{\gamma/\rho g}$ is the capillary length. Figure S2b is obtained using the following physical properties of 0.1M KOH electrolyte - γ

3

=72.85 mN m^{-1}, ρ =1000 kg m^{-3}, and θ =0 (perfect wetting). The discontinuous slope of meniscus at the horizontal distance (or film thickness) of 30 µm is due to change in the surface tension of gas-liquid interface as it gets closer to the electrode. According to the experimental observation, the film thickness of ~30 nm is achieved at a height of ~7 mm. From the force balance equations (S2 and S3), the meniscus height of 7 mm requires surface tension to be 234.69 mN m^{-1}, which is 3.2 times higher than the bulk value 72.85 mN m^{-1}. If we assume the surface tension increases linearly from 72.85 mN m^{-1} at 3.5 mm height to 234.69 mN m^{-1} at 7 mm height, the thickness of meniscus can be obtained using equation S3. This surface-tension gradient of 46.24 Pa pulls the liquid in the thin-film in upward direction, which causes convection in the thin-film known as Marangoni effect.

The governing equations and boundary conditions required to obtain the distributions of current density, pH, and solution losses along the height of the thin-film are discussed below.
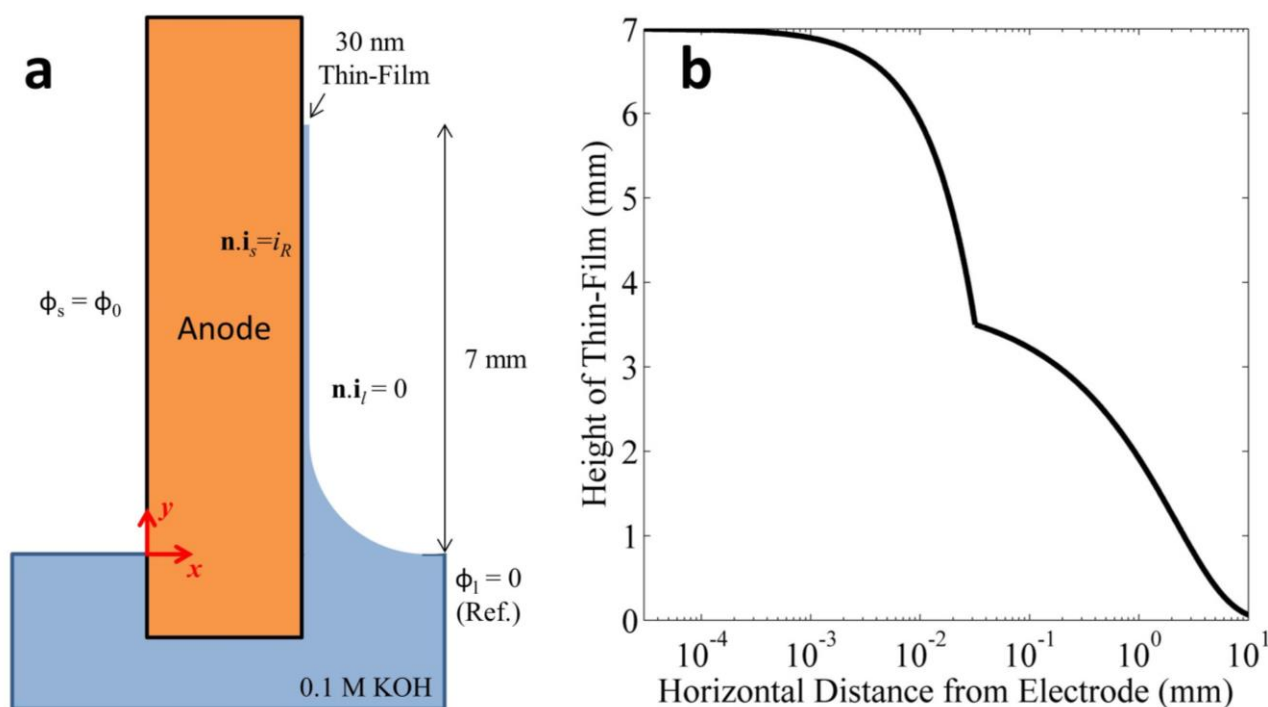

Figure S3. (a) Schematic diagram of a "dipstick" electrochemical cell showing dimensions of thin-film and boundary conditions, (b) liquid meniscus profile of 0.1M KOH on a hydrophilic surface.

Mass and Charge Balance

The transport of species such as K^{+}, OH^{-} and H^{+} in the thin-film must satisfy mass conservation, such that

$$\frac{\partial c_i}{\partial t} + \nabla \cdot \mathbf{N}_i = R_i \qquad (S4)$$

where $\mathbf{N}_i$ is a 2D vector of molar flux, R_i is the volumetric rate of formation of species i, x is the position along width of the film, and y is the position along the height of the film. The rate of formation of H^+ and OH^- can be determined from the bulk ionization of water,

$$H_2O \rightleftharpoons H^+ + OH^-$$
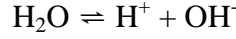
where the value of the forward rate constant of water ionization is $k_{+w} = 2.4 \times 10^{-5} \, \text{mol} \, \text{L}^{-1} \, \text{s}^{-1}$ and the equilibrium constant is $K_w = 1 \times 10^{-14} \, \text{mol}^2 \, \text{L}^{-2}$.[3]

The molar flux of species in dilute electrolyte can be written as a sum of fluxes due to diffusion and migration.

$$\mathbf{N}_i = -D_i \nabla c_i - z_i u_i F c_i \nabla \phi_l + c_i \mathbf{v} \qquad (S5)$$

where F is Faraday's constant, z_i is the charge number, D_i is the diffusion coefficient, c_i is the concentration of the ith species, u_i is the mobility of ions given by the Nernst-Einstein relationship, ϕ_l is the electrolyte potential, and $\mathbf{v}$ is the velocity due to Marangoni effect. The velocity field is obtained by solving a two-dimensional Navier-Stokes equation in the thin-film using no-slip boundary condition at the electrode-liquid interface and fixed-stress boundary condition at the gas-liquid interface. The interfacial stress at the gas-liquid interface is equal to the value of surface-tension gradient of 46.24 Pa (described below equation S3). The surface-tension gradient causes velocity field along y-direction (upward direction) as a function of x-direction, this phenomenon is known as Marangoni effect. The continuous flow of liquid in the upward direction is supported by continuous evaporation of the thin-film.

The diffusion coefficients of species in the dilute electrolyte are given in Table S1. We neglect the variation of diffusion coefficients with the electrolyte concentration, as the variation is marginal for dilute electrolytes (< 10 mol%).[4]

Table S1: Diffusion coefficients of species in water at infinite dilution at 25 ℃ [5,6]

Species	Diffusion Coefficient ($10^{-9} \, \text{m}^2 \, \text{s}^{-1}$)	Mobility ($10^{-7} \, \text{m}^2 \, \text{V}^{-1} \, \text{s}^{-1}$)
H^+	9.311	3.626
OH^-	5.273	2.054
K^+	1.957	0.762

Electrolyte Current Density

The electrolyte current density vector $\mathbf{i}_l$ can be obtained from the total ionic flux,
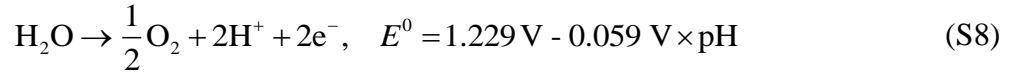
$$\mathbf{i}_l = F \sum_i z_i \mathbf{N}_i \qquad (S6)$$

and the assumption of electro-neutrality,

$$\sum_i z_i c_i = 0 \qquad (S7)$$

Water Oxidation at Anode

The half-cell reaction at the anode is the oxidation of water, which reduces alkalinity near the electrode.

$$H_2O \rightarrow \frac{1}{2}O_2 + 2H^+ + 2e^-, \quad E^0 = 1.229\,\text{V} - 0.059\,\text{V} \times \text{pH} \qquad (S8)$$

The measured cyclic voltammogram was used as is (without fitting it to a kinetic expression) to model the kinetics of water oxidation on NiFe, such that

$$\mathbf{n} \cdot \mathbf{i}_s = -\mathbf{n} \cdot \mathbf{i}_l = i_R = f(\eta) \qquad (S9)$$

where $\mathbf{n}$ is a normal vector point outward from the domain, i_R is the reaction current density, $\mathbf{i}_s$ is the electrode current density, ϕ_s is the electrode potential, and f is the interpolated function of the kinetic overpotential, $\eta = \phi_s - \phi_l - E^0$, which was derived from the cyclic voltammogram data.

Electrode Current Density

The current density at a metal electrode is given by Ohm's law:

$$\mathbf{i}_s = -\kappa_s \nabla \phi_s \qquad (S10)$$

where κ_s is the conductivity of the electrode.

To maintain electroneutrality, the divergence of current density in the solid and the liquid must be zero:

$$\nabla \cdot \mathbf{i}_l = 0, \quad \nabla \cdot \mathbf{i}_s = 0 \qquad (S11)$$

The potential in the electrochemical cell was calculated relative to a Ag/AgCl reference electrode potential near anode, and the anode potential was fixed to 0.3 V, 0.55 V and 0.6 V according to the XPS measurements.

Boundary Conditions at Gas-Liquid Interface

The gas-liquid interface of thin-film as shown in Figure 1a was modeled as an insulator.

$$\mathbf{n} \cdot \mathbf{i}_l = 0 \qquad (S12)$$

Computation

Equations S2-S13 were solved using COMSOL Multiphysics 4.3b. The solution loss, sum of ohmic and diffusion losses, was obtained as follows:

$$\Delta\phi_{solution} = \underbrace{\oint_s \frac{\mathbf{t}\cdot\mathbf{i}_l}{\kappa}ds}_{\Delta\phi_{ohmic}} + \underbrace{\sum_i \oint_s \frac{Fz_iD_i\,\mathbf{t}\cdot\nabla c_i}{\kappa}ds}_{\Delta\phi_{diffusion}} \qquad (S13)$$

where $\mathbf{t}$ is a tangent vector along the gas-liquid interface of the thin-film, and s is the arc length of the same interface.

The half-cell potential can be written as a sum of equilibrium potential, kinetic overpotential and the solution loss:

$$\mathrm{V} = E^0 + \eta + \Delta\phi_{solution} \qquad (S14)$$

The shift in the binding energy of water corresponds to the difference between the electrolyte and electrode potential, which is also the potential requirement for water oxidation, such that

$$-\Delta\phi_{BE} = \phi_s - \phi_l = E^0 + \eta = \mathrm{V} - \Delta\phi_{solution} \qquad (S15)$$

Distribution of Potential, pH, and Current Density in the Thin-Film

Figure S4 shows the variation in the equilibrium potential, kinetic overpotential, and solution losses, as a function of the height of thin-film at an applied potential of 0.3 V and 0.55 V vs Ag/AgCl. It can be seen that the solution losses are negligible till the electrode height of 3.5 mm. The solution loss increases slightly by ~0.7 mV at the applied potential of 0.3 V near the electrode height of 7 mm. When the applied potential at 7 mm height is increased to 0.55 V, the solution loss, equilibrium potential, and kinetic overpotential are 44.8 mV, 315.3 mV, and 189.8 mV respectively. Consequently, the current density and pH, as shown in Figure S5, drop down to 8 μA cm^{-2}, and 12.15, respectively. From equation (S16), the shift in the binding energy is equal to the sum of equilibrium potential and kinetic overpotential at the electrode height of 7mm. The increase in the equilibrium potential with the electrode height is due to slight decrease in the pH, which is shown in Figure S5b.
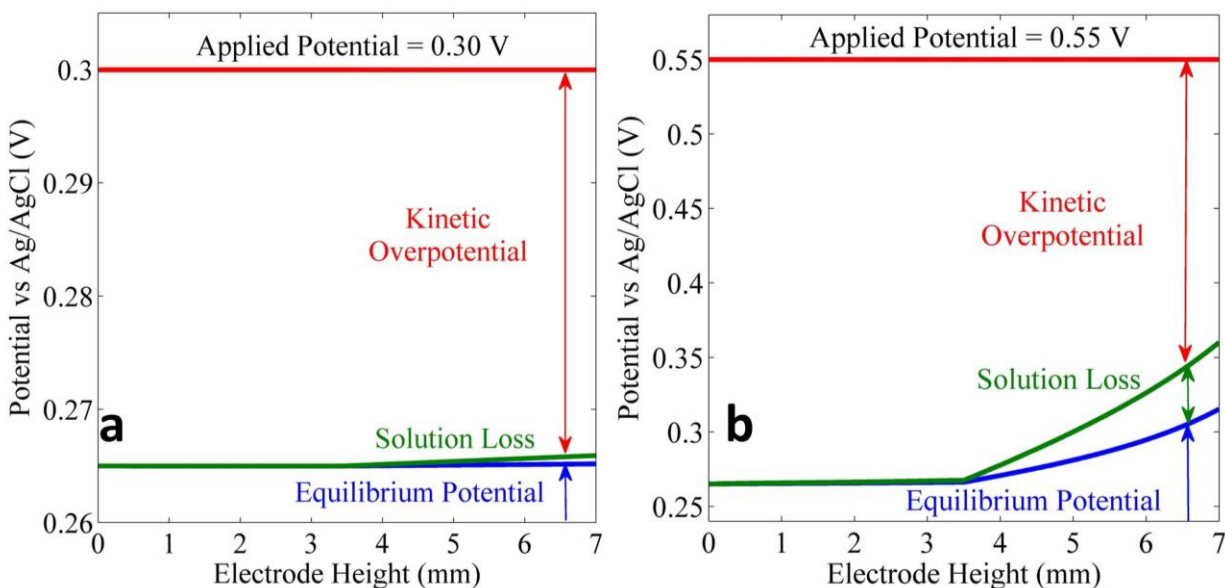
Figure S4. Variation of kinetic overpotential, solution loss, and equilibrium potential along the height of the electrode at the applied potential of 0.3 V and 0.55 V vs Ag/AgCl.
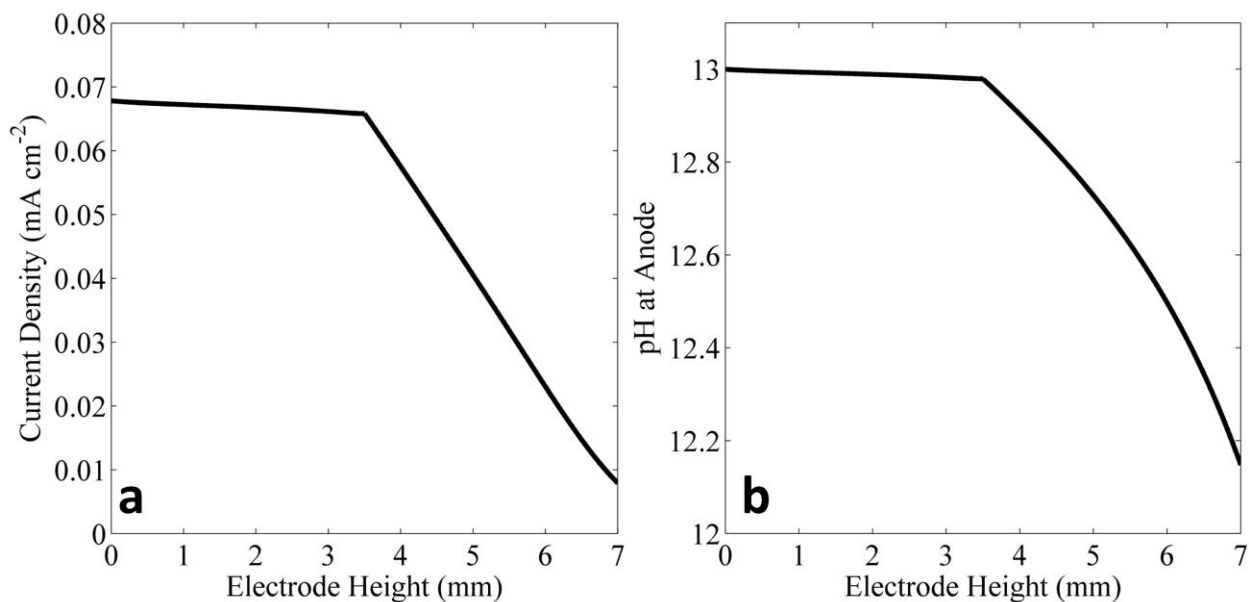

Figure S5. (a) Current density, (b) anode pH versus electrode height at an applied potential of 0.55 V vs Ag/AgCl.

Energy Band Diagram of the Electrochemical Cell

Figure S6 shows the energy diagram for the electrochemical cell for three different applied potentials E^{WE} of 0, 0.3 and 0.55 V vs. Ag/AgCl. Since the working electrode (WE) and

the XPS analyzer are both connected to electric ground, the Fermi energy E_F is the constant reference point for all binding energies. By changing the applied potential by ΔE^{WE}, we change, by the same amount, the work function of the WE per electronic charge e: $\Delta \Phi^{WE}/e = \Delta E^{WE}$. This does not affect the binding energies of states within the WE, since these are constant with respect to E_F. By contrast, gas phase species are expected to have constant core level ionization energies IE^{gas} with respect to the vacuum level. The latter shifts with the work function change of the WE (for simplicity, we neglect here the small deviation from this 1:1 relationship that are due to the distribution of excited gas molecules between sample and analyzer), and therefore, a work function increase results in a decrease of the *apparent* O1s binding energy of $H_2O(g)$. The same behavior is also expected for the apparent O1s BE of liquid water in the electrolyte if potential losses in the electrolyte are negligible, as is the case during the potential increase from 0 to 0.3 V. Upon further potential increase to 0.55 V, the ohmic drop iR in the thin electrolyte layer becomes significant and causes core-level ionized H_2O to experience an additional electric potential of iR and its ionization energy is therefore increased by eiR. Accordingly, the decrease of apparent binding energy of $H_2O(l)$ is smaller and deviates significantly from that for $H_2O(g)$ under the same applied potential.
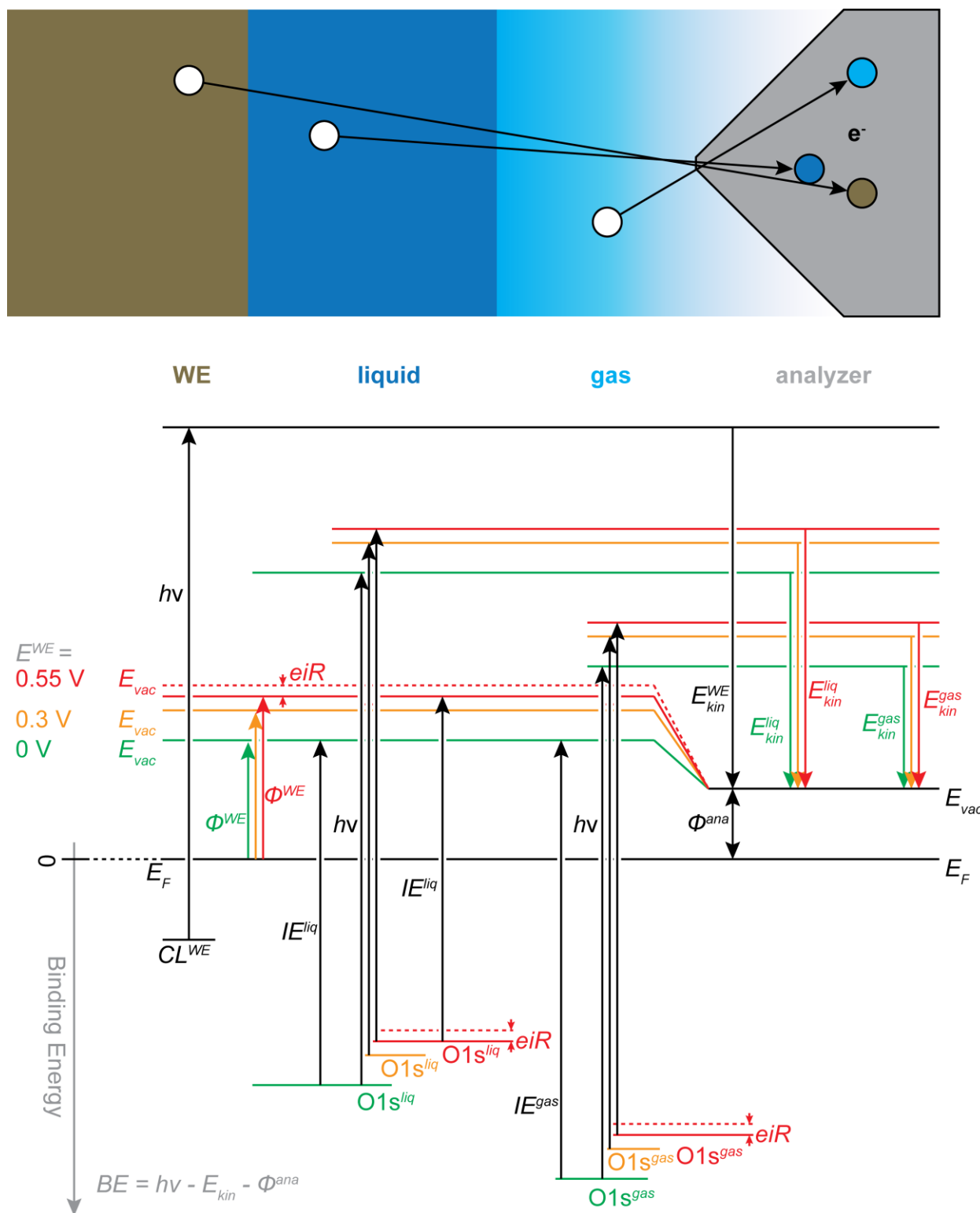
Figure S6. Energy diagram of the anode/electrolyte interface at different applied potentials, showing transitions from core levels in the working electrode (CL^{WE}), from water in the liquid electrolyte ($O1s^{liq}$) and from water in the gas phase ($O1s^{gas}$) upon excitation with the x-ray energy $h\nu$, resulting in photoelectrons that are detected at kinetic energies E_{kin}^{WE}, E_{kin}^{liq}, and E_{kin}^{gas}.

E_{vac} is the energy of electrons in vacuum, E_F is the Fermi energy, Φ^{WE} and Φ^{ana} are the work functions in close proximity to the working electrode and the XPS analyzer, respectively. A color scheme is used to distinguish energy levels (horizontal lines) and transitions (vertical arrows) that are constant (black), or that change with applied potential (green/orange/red).

Absence of potential-induced Au oxide formation

Figure S7 shows the background-subtracted and normalized Au 4f XP spectra of the as-prepared sample at 9 Torr H_2O pressure, and at applied potentials of 0.3 V and 0.55 V vs. Ag/AgCl in 0.1 M KOH. All three spectra have identical line shapes characteristic of Au in the metallic state. Au oxide formation would give rise to an additional component at 85 eV and 89 eV, which is not observed.
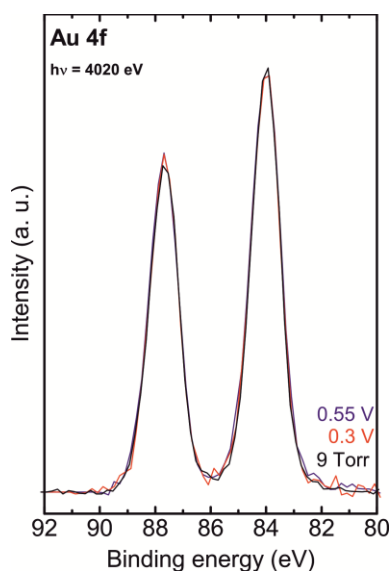

Figure S7. Comparison of XP spectra in the Au 4f region, measured on the as-prepared sample and at applied potentials of 0.3 V and 0.55 V vs. Ag/AgCl in 0.1 M KOH.

Similarity of M–O and M–OH peaks before and after electrochemical conditioning

In Figure S8 we show the fitted components for O 1s spectra at 0.0 and 0.3 V, each recorded before and after the second electrochemical conditioning (potential cycles 0-0.85 V). The electrochemical conditioning only affects the $H_2O(l)$ peak position, otherwise identical trends can be seen when going from 0 to 0.3 V: shift of both H_2O components by ~0.3 V, and increase of the ratio between M–O and M–OH peak intensities.
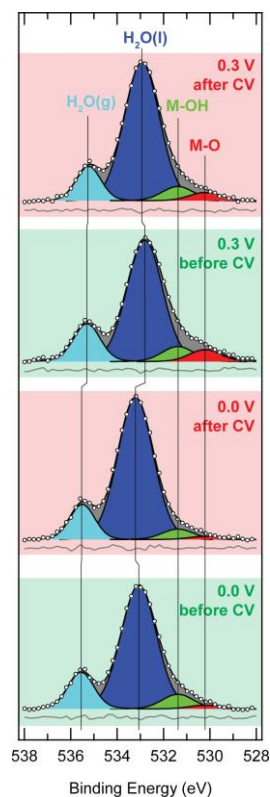
Figure S8. Comparison of XP spectra in the O1s region, recorded at 0.0 V and 0.3 V, with fitted components. For each potential, data recorded before and after electrochemical conditioning (potential cycling 0-0.85 V) are shown.

References

(1) Newberg, J. T.; Starr, D. E.; Yamamoto, S.; Kaya, S.; Kendelewicz, T.; Mysak, E. R.; Porsgaard, S.; Salmeron, M. B.; Jr, G. E. B.; Nilsson, A.; et al. Formation of Hydroxyl and Water Layers on MgO Films Studied with Ambient Pressure XPS. *Surf. Sci.* **2011**, *605* (1-2), 89–94.

(2) Couto, P. C. do; Cabral, B. J. C. Electronically Excited Water Aggregates and the Adiabatic Band Gap of Water. *J. Chem. Phys.* **2007**, *126* (1), 014509.

(3) Atkins, P.; Paula, J. de. *Atkins' Physical Chemistry*, Tenth Edition.; Oxford University Press, 2014.

(4) Newman, J.; Thomas-Alyea, K. E. *Electrochemical Systems*; John Wiley & Sons, 2012.

(5) Flury, M.; Gimmi, T. Solute Diffusion. In *Methods of Soil Analysis. Part 4. Physical Methods*; Dane, J. H., Clarke, C., Eds.; Soil Science Society of America: Madison, Wis, 2002; pp 1323–1351.

(6) Jähne, B.; Heinz, G.; Dietrich, W. Measurement of the Diffusion Coefficients of Sparingly Soluble Gases in Water. *J. Geophys. Res. Oceans* **1987**, *92* (C10), 10767–10776.